Neurologic 3D MR Spectroscopic Imaging with Low-Power Adiabatic Pulses and Fast Spiral Acquisition[1]

Ovidiu C. Andronesi, MD, PhD
Borjan A. Gagoski, PhD
A. Gregory Sorensen, MD[2]

Purpose: To improve clinical three-dimensional (3D) MR spectroscopic imaging with more accurate localization and faster acquisition schemes.

Materials and Methods: Institutional review board approval and patient informed consent were obtained. Data were acquired with a 3-T MR imager and a 32-channel head coil in phantoms, five healthy volunteers, and five patients with glioblastoma. Excitation was performed with localized adiabatic spin-echo refocusing (LASER) by using adiabatic gradient-offset independent adiabaticity wideband uniform rate and smooth truncation (GOIA-W[16,4]) pulses with 3.5-msec duration, 20-kHz bandwidth, 0.81-kHz amplitude, and 45-msec echo time. Interleaved constant-density spirals simultaneously encoded one frequency and two spatial dimensions. Conventional phase encoding (PE) (1-cm^3 voxels) was performed after LASER excitation and was the reference standard. Spectra acquired with spiral encoding at similar and higher spatial resolution and with shorter imaging time were compared with those acquired with PE. Metabolite levels were fitted with software, and Bland-Altman analysis was performed.

Results: Clinical 3D MR spectroscopic images were acquired four times faster with spiral protocols than with the elliptical PE protocol at low spatial resolution (1 cm^3). Higher-spatial-resolution images (0.39 cm^3) were acquired twice as fast with spiral protocols compared with the low-spatial-resolution elliptical PE protocol. A minimum signal-to-noise ratio (SNR) of 5 was obtained with spiral protocols under these conditions and was considered clinically adequate to reliably distinguish metabolites from noise. The apparent SNR loss was not linear with decreasing voxel sizes because of longer local T2* times. Improvement of spectral line width from 4.8 Hz to 3.5 Hz was observed at high spatial resolution. The Bland-Altman agreement between spiral and PE data is characterized by narrow 95% confidence intervals for their differences (0.12, 0.18 of their means). GOIA-W(16,4) pulses minimize chemical-shift displacement error to 2.1%, reduce nonuniformity of excitation to 5%, and eliminate the need for outer volume suppression.

Conclusion: The proposed adiabatic spiral 3D MR spectroscopic imaging sequence can be performed in a standard clinical MR environment. Improvements in image quality and imaging time could enable more routine acquisition of spectroscopic data than is possible with current pulse sequences.

[1] From the Martinos Center for Biomedical Imaging, Department of Radiology, Massachusetts General Hospital, Harvard Medical School, 149 13th St, Suite 2301, Boston, MA 02129 (O.C.A., A.G.S.); and Department of Electrical Engineering and Computer Science, Massachusetts Institute of Technology, Cambridge, Mass (B.A.G.). Received February 7, 2011; revision requested March 30; revision received August 16; accepted August 30; final version accepted September 6. Supported by the Siemens–Massachusetts Institute of Technology Alliance. **Address correspondence to** O.C.A. (e-mail: *ovidiu@nmr.mgh.harvard.edu*).

[2] **Current address:** Siemens Healthcare, Malvern, Pa.

In vivo magnetic resonance (MR) spectroscopic imaging (also known as chemical-shift imaging) yields detailed metabolic information that correlates with normal physiology or disease. MR spectroscopic imaging shows the potential to improve diagnosis or treatment follow-up compared with other imaging techniques for many conditions (1–4), including brain tumors, stroke, and psychiatric disorders, especially when invasive (biopsy) and other serial metabolic imaging (positron emission tomography, single photon emission computed tomography [5]) investigations are limited. However, MR spectroscopic imaging is not universally reimbursed by payers because its clinical utility has not been established unequivocally. This last aspect could in part be related to limited data quality due to reduced spatial coverage, low spatial resolution, long acquisition times, and localization artifacts when standard pulse sequences are used with clinical systems.

Advances in Knowledge

- Optimized adiabatic pulses, having lower power requirements, larger bandwidth, and shorter durations than typical hyperbolic secant pulses, can minimize artifacts, such as chemical-shift displacement error, nonuniform excitation, and lipid contamination.
- Spiral readout trajectories simultaneously acquire the frequency dimension and two of the spatial dimensions and can accelerate collection of spectroscopic data by up to 50 times, provided signal-to-noise ratio (SNR) is not a limiting factor.
- Four times shorter imaging times or 85% smaller real voxel size in half of the imaging time as compared with those used to acquire elliptical phase-encoded data can be acquired with spiral encoding with a corresponding lower but still clinically adequate SNR (>5); SNR decreases in a less-than-linear fashion with spatial resolution, while spectral line width improves.

MR spectroscopic imaging presents several challenges that prevent us from harvesting its full potential. Important limitations result from the use of conventional radiofrequency pulses (6) that have large chemical-shift displacement error and nonuniform excitation, as well as from the use of slow phase-encoding schemes (7) without readout gradients that require long acquisition times and yield low spatial resolution.

Adiabatic excitation, such as localized adiabatic spin-echo refocusing (LASER), (8) can mitigate the drawbacks of conventional radiofrequency pulses. Recently optimized gradient-offset independent adiabaticity wideband uniform rate and smooth truncation (GOIA-W[16,4]) pulses (9) make this approach feasible with clinical imagers for reduction of chemical-shift displacement error to 2.1% and nonuniformity to 5% with low power requirements (specific absorption rate [SAR]) that permit the use of short echo (45 msec) and repetition (1.0–1.25 sec) times. Constant density gradient waveforms played during readout can accelerate MR spectroscopic imaging (10) along two of the three spatial dimensions, resulting in significantly shorter acquisition times (at least 50 times shorter) compared with conventional phase encoding. However, in clinical three-dimensional (3D) MR spectroscopic imaging of the human brain, some of the spiral acceleration factor can be traded off for increased signal-to-noise ratio (SNR) with additional signal acquisition, enabling a more flexible choice of imaging matrix and examination time.

Performance of spiral 3D MR spectroscopic imaging (10) was compared with performance of conventional phase-encoding 3D MR spectroscopic imaging (7) by using the same adiabatic excitation (9). In particular, to our knowledge, the benefit of combining adiabatic excitation and spiral encoding has not been well documented for spectroscopic imaging (11,12). Typically, most clinical 3D MR spectroscopic imaging performed with conventional phase encoding uses elliptical k-space acquisition (13). We chose elliptical phase encoding as the reference standard for comparison with spiral encoding because full phase encoding of 3D MR spectroscopic imaging would result in imaging times that were too long and clinically impractical, even for a modest matrix of $16 \times 16 \times 8$. In optimizing spiral encoding, an acquisition time of 5 minutes

Implication for Patient Care

- The ability to obtain high-quality important metabolic information with extended spatial coverage and higher spatial resolution in feasible imaging times may facilitate the acquisition of spectroscopic data on a routine basis in clinical practice.

Published online before print
10.1148/radiol.11110277 **Content codes:** NR MR

Radiology 2012; 262:647–661

Abbreviations:
AP-RL-HF = anterior-posterior right-left head-feet
FOV = field of view
GOIA-W(16,4) = gradient-offset independent adiabaticity wideband uniform rate and smooth truncation
LASER = localized adiabatic spin-echo refocusing
NAA = *N*-acetyl-L-aspartic acid
NAA/Sum = index of NAA over the sum of all metabolites
PSF = point spread function
SAR = specific absorption rate
SNR = signal-to-noise ratio
SP1 = spiral protocol 1
SP2 = spiral protocol 2
SP3 = spiral protocol 3
SP4 = spiral protocol 4
SP5 = spiral protocol 5
SP6 = spiral protocol 6
3D = three-dimensional
VOI = volume of interest

Author contributions:
Guarantor of integrity of entire study, O.C.A.; study concepts/study design or data acquisition or data analysis/interpretation, all authors; manuscript drafting or manuscript revision for important intellectual content, all authors; manuscript final version approval, all authors; literature research, O.C.A.; clinical studies, all authors; experimental studies, O.C.A., B.A.G.; statistical analysis, O.C.A.; and manuscript editing, all authors

Funding:
This research was supported by the National Institutes of Health (grants R01 1200-206456, R01EB007942, and R01EB006847).

Potential conflicts of interest are listed at the end of this article.

or less was thought to be desirable for clinical 3D MR spectroscopic imaging, considering that some additional time is spent on shim and water suppression adjustments. We used the flexible tradeoff of imaging time, spatial resolution, and averaging with spiral MR spectroscopic imaging to investigate the combination of spatial resolution and examination time that yields sufficient SNR for clinical use. Faster acquisition times and higher spatial resolution are seen with adiabatic spiral 3D MR spectroscopic imaging protocols while imposing a minimum SNR larger than 5 for any metabolite, considered here to be clinically adequate.

We present results from phantoms, volunteers, and patients with brain tumors obtained with such an approach. The purpose of this study was to improve clinical 3D MR spectroscopic imaging with more accurate localization and faster acquisition schemes.

Materials and Methods

One author (B.A.G.) received partial funding from the Siemens–Massachusetts Institute of Technology Alliance. Another author (A.G.S.) served as a consultant for Siemens Medical Solutions (Erlangen, Germany) and changed his affiliation to Siemens Healthcare after the manuscript had been submitted for publication. Neither author had control of the data or information submitted for publication. The remaining author (O.C.A.) did not have any industry employment or consulting responsibilities and therefore was the only author who performed measurements and had control of data inclusion.

MR Spectroscopic Imaging of Phantoms

For each 3D MR spectroscopic protocol, the following aspects were investigated in a double-layer phantom and a uniform phantom: localization and lipid contamination in the double-layer phantom and uniformity of excitation and SNR limits for high-spatial-resolution data in the uniform phantom.

A large homogeneous spherical phantom (16-cm inner diameter) that contained brain metabolites at physiologic concentrations and a double-layer cylindrical phantom that had an outer ring of oil (2-cm thickness) and an inner core (8.5-cm inner diameter) with brain metabolites were used for preliminary tests. The brain metabolites in both phantoms were as follows: 12.5 mmol/L of *N*-acetyl-L-aspartic acid (NAA), 10 mmol/L of creatine hydrate, 3 mmol/L of choline chloride, 7.5 mmol/L of myo-inositol, 12.5 mmol/L of L-glutamic acid, and 5 mmol/L of DL-lactic acid, which were treated with sodium azide (0.1%) to prevent bacterial growth. They were pH buffered with 50 mmol/L of monobasic potassium phosphate, 56 mmol/L of sodium hydroxide, and 1 mL/L of gadopentetate dimeglumine (Magnevist; Bayer Schering Pharma, Berlin, Germany) to obtain T1 relaxation times similar to those in vivo.

The total number of signals acquired and the acquisition time for three matrixes ($16 \times 16 \times 8$, $22 \times 22 \times 12$, and $30 \times 30 \times 14$) are given in Table 1 for elliptical phase-encoding, full phase-encoding, and spiral encoding protocols, respectively. In each 3D matrix, the larger dimensions were spiral encoded. The matrix sizes were generated with the spiral trajectory algorithm within gradient slew rate and amplitude constraints to obtain in-plane spatial resolutions of 1 cm^2 ($16 \times 16 \times 8$ matrix), 0.5 cm^2 ($22 \times 22 \times 12$ matrix), and 0.25 cm^2 ($30 \times 30 \times 14$ matrix). The spatial resolution along the third dimension was chosen to have an isotropic voxel. For phase encoding, the only protocol that would yield a clinically feasible acquisition time was the elliptical phase-encoded $16 \times 16 \times 8$ matrix.

We compared 3D MR spectroscopic imaging data obtained by using one elliptical phase-encoding protocol ($16 \times 16 \times 8$ matrix, one signal acquired) with 3D MR spectroscopic imaging data acquired by using five spiral encoding protocols. For spiral protocol 1 (SP1), we used the same matrix ($16 \times 16 \times 8$) and 12 signals acquired that give the same acquisition time as in the case of the elliptical phase-encoding protocol. For spiral protocol 2 (SP2), we used the same matrix, but the acquisition time was two times faster ($16 \times 16 \times 8$ matrix, six signals acquired). For spiral protocol 3 (SP3), we used the same matrix as for SP2, but the acquisition time was four times faster ($16 \times 16 \times 8$ matrix, three signals acquired). For spiral protocol 4 (SP4), we used higher spatial resolution, and acquisition time was two times faster ($22 \times 22 \times 12$ matrix, three signals acquired). For spiral protocol 5 (SP5), we used the highest spatial resolution, and acquisition time was two times faster ($30 \times 30 \times 14$ matrix, one signal acquired). The field of view (FOV) in the anterior-posterior right-left head-feet (AP-RL-HF) direction was $160 \times 160 \times 80$ mm for low-spatial-resolution protocols ($16 \times 16 \times 8$ matrix, 10 mm isotropic voxel), $160 \times 160 \times 88$ mm for medium-spatial-resolution protocols ($22 \times 22 \times 12$ matrix, 7.3 mm isotropic voxel), and $160 \times 160 \times 74$ mm for high-spatial-resolution protocols ($30 \times 30 \times 14$ matrix, 5.3 mm isotropic voxel). The data acquired with $22 \times 22 \times 12$ and $30 \times 30 \times 14$ matrixes were interpolated to a $32 \times 32 \times 16$ matrix before reconstruction. LASER selection of the volume of interest (VOI) with an echo time of 45 msec was used for all phase-encoded and spiral protocols. The same repetition time, 1000 msec, was used in all experiments. Localizer images were used to position the VOI. B_0 shimming was performed with the advanced shimming routine (Siemens, Erlangen, Germany) until a line width of 5 Hz (magnitude mode) or better was obtained for the water signal.

MR Spectroscopic Imaging in Patients and Control Subjects

A physicist and physician (O.C.A.) with 9 years of MR experience performed 3D MR spectroscopic imaging of the brain in five healthy volunteers (three men, two women; age range, 21–30 years; median age, 26 years) and five patients with brain tumors (four men, one woman; age range, 24–65 years; median age, 59.5 years). The patients were selected by a neuroradiologist (A.G.S., with more than 20 years of experience) after a diagnosis of glioblastoma multiforme was made at

Table 1

Acceleration Factors for Cylindrical Stack-of-Spirals Compared with Full and Elliptical Phase-Encoding of 3D MR Spectroscopic Imaging

	3D MR Spectroscopic Imaging with Stack-of-Spirals Method			3D MR Spectroscopic Imaging with Phase-Encoding Method		
3D Matrix	No. of Angular Interleaves	No. of Temporal Interleaves	No. of Spiral Excitations	No. of Full Phase-Encoding Excitations	No. of Elliptical Phase-Encoding Excitations	Spiral Acceleration*
16 x 16 x 8	3	2	48 (48 sec)	2048 (34 min 8 sec)	603 (10 min 3 sec)	43, 13
22 x 22 x 12	6	2	144 (2 min 24 sec)	5808 (1 h 36 min 48 sec)	2047 (34 min 7 sec)	40, 14
30 x 30 x 14	6	3	252 (4 min 12 sec)	12600 (2 h 10 min)	4889 (1 h 21 min 29 sec)	50, 19

Note.—Spiral encoding can make image acquisition 50 times faster and allow high-spatial-resolution 3D spectroscopic images to be obtained with a feasible imaging time. The z direction is phase encoded in all protocols. Data in parentheses are acquisition times for each protocol and assume the same number of signals acquired (one average) and repetition time (1000 msec).

* Data are for full phase-encoding protocol compared with elliptical phase-encoding protocol.

histopathologic examination. The inclusion criteria (A.G.S.) required identification of a tumor with a diameter of at least 1 cm on the contrast material–enhanced T1-weighted image. Patients with tumors that had large areas of blood products because of postbiopsy hemorrhage were excluded. Studies involving human subjects were approved by the Massachusetts General Hospital institutional review board.

Comparisons were made between 3D MR spectroscopic images obtained with the elliptical phase-encoding protocol (16 × 16 × 8 matrix, one signal acquired) and those acquired with four spiral encoding protocols (SP2, SP3, SP4, and SP6). For SP2, SP3, and SP4, the parameters were the same as those described earlier in this article. For spiral protocol 6 (SP6) tested in volunteers, we used a 22 × 22 × 12 matrix and six signals were acquired, which yielded an acquisition time similar to that obtained with the elliptical phase-encoding protocol. Because of time constraints to patients, only the shorter spiral protocols (SP2–SP4) were performed. The acquisition time, matrix, and voxel size corresponding to each protocol are given in Table 2. The FOV was 160 × 160 × 80 mm in the AP-RL-HF direction for low-spatial-resolution protocols (16 × 16 × 8 matrix, 10 mm^3 isotropic voxel), and 160 × 160 × 88 mm in the AP-RL-HF direction for high-spatial-resolution protocols (22 × 22 × 12 matrix, 7.3 mm^3 isotropic voxel). Data obtained with a 22 × 22 × 12 matrix were zero-filled to a matrix of 32 × 32 × 16 before reconstruction. LASER selection of the VOI with a 45-msec echo time was used for all protocols. A repetition time of 1000 msec was used in all subjects with the exception of one volunteer who required a repetition time of 1200 msec because of SAR of the LASER sequence.

Images used to position the VOI were acquired with the multiecho magnetization-prepared rapid acquisition gradient-echo (14) sequence (repetition time msec/echo times msec/inversion time msec, 2530/1.64, 3.5, 5.36, 7.22/1200; 1 mm^3 isotropic voxel) in volunteers and the aforementioned multiecho magnetization-prepared rapid acquisition gradient-echo sequence after contrast material injection in patients with tumors. B_0 shimming of the entire VOI was performed with the advanced shimming routine until a line width of 16 Hz (magnitude mode) or better was obtained for the water signal.

Hardware and Sequence Programming

All measurements were performed by one researcher (O.C.A.) using a 3-T Magnetom Tim Trio system (Siemens). The body coil was used for transmission, and the 32-channel phased-array head coil was used to receive the signal. The maximum amplitude of the B_1 field delivered by the transmit body coil is typically limited to 1 kHz (23.6 μT). The gradient system specifications include a maximum amplitude of 26 mT/m and a maximum slew rate of 170 mT/(m·msec).

GOIA-W(16,4) pulses with a 3.5-msec duration, 20-kHz bandwidth, and 0.817-kHz maximum B_1 field were used for LASER. Amplitude, gradient, and phase modulations (9) based on wideband uniform rate and smooth truncation (15) were calculated online (O.C.A) with the imager pulse sequence software (IDEA VB17A; Siemens). Gradient spoilers of 10- and 8-mT/m amplitude and 1.9-msec total duration (700-μsec ramp-up and ramp-down times, 500-μsec flat top) were used. The minimum echo time with these parameters was 43.8 msec, which was rounded up to 45 msec by inserting small symmetric delays (100 μsec) around each pulse. The signal was excited initially with a 90° nonselective adiabatic half-passage pulse based on offset independent adiabaticity eigth-order hyperbolic secant (16) modulation with a duration of 4 msec and a 5-kHz bandwidth. No outer volume suppression of lipids was necessary because of precise LASER excitation (8,9). Water suppression was realized with a water suppression enhanced through T1 effects scheme (17) in all sequences.

Spiral gradients (n = 380) were played simultaneously on the read- and phase-gradient channels for spectroscopic imaging of the excited VOI. The spectral bandwidth for all acquisitions was set to 1.2 kHz, which corresponded to 9.75 ppm at 3 T. The spiral gradients played within one repetition time are identical to get the time evolution of the chemical shift, while interleaved spiral trajectories must be played in

Table 2

In Vivo 3D MR Spectroscopic Imaging and Comparison of Imaging Protocols, Voxel Size, and SNR

3D MR Spectroscopic Imaging Protocol	Matrix	No. of Signals Acquired	Acquisition Time	Voxel Size (cm^3)		SNR Scaling Factor	SNR in Vivo				
				FOV-to-Matrix Ratio	PSF		NAA	Choline	Creatine	Glutamate and Glutamine	*myo*-Inositol
Elliptical phase encoding	16 x 16 x 8	1	10 min 7 sec	1	4.28	1.0	121	40.7	59.7	32.8	41.7
SP2	16 x 16 x 8	6	4 min 50 sec	1	1.26	5.3	35.3	11.7	19.7	10.4	14.5
SP3	16 x 16 x 8	3	2 min 25 sec	1	1.26	7.5	20.7	6.68	11.8	6.75	6.74
SP4	22 x 22 x 12	3	4 min 48 sec	0.39	0.66	10.2	12.2	6.71	7.18	5.53	5.10
SP6	22 x 22 x 12	6	9 min 36 sec	0.39	0.66	7.2	21.1	7.26	11.8	6.56	9.41

Note.—Stack-of-spirals and elliptical phase-encoding 3D MR spectroscopic imaging protocols used to acquire in vivo data, indicating the matrix, number of signals acquired, acquisition time, and voxel size (nominal image-based voxel size as FOV-to-matrix ratio and real voxel size as integral of the PSF). The SNR scaling factor is estimated based on the PSF, square root of time, rewinder duration, and number of points in the free induction decay. In vivo SNR was determined by using standard deviation of noise in a spectral region free of signal and the maximum signal intensity for each metabolite.

consecutive repetition times to cover the desired FOV and spectral bandwidth (SW) (10). The required FOV, spatial resolution (matrix size), and spectral bandwidth are obtained by modifying the duration of each spiral lobe concomitant with the number of angular interleaves (for changing FOV and spatial resolution d_x, d_y) and the number of temporal interleaves (for changing spectral bandwidth). Angular interleaving decomposes the k_x and k_y space into sparser N_a spiral trajectories rotated by an angle $\theta_n = (n-1)2\pi/N_a \ \left(n = \overline{1, N_a}\right)$. For temporal interleaving, the readout gradients start $(n-1)\cdot 1/\mathrm{SW}$ seconds $\left(n = \overline{1, N_t}\right)$ later relative to the apparent start of the analog to digital converter. The choice of angular (N_a) or temporal (N_t) interleaves is made such that acquisition time $\left(\mathrm{TA} = N_a \cdot N_t \cdot \mathrm{TR}\right)$, where TR is repetition time, is minimized. A rewinder gradient is used after each spiral gradient to return to the origin of k-space, with the duration of the rewinder fixed to the shortest value. For all protocols, constant density spiral trajectories were designed so that the number of temporal interleaves did not exceed three and the length of the rewinder gradient was not more than 15% of the total duration of the spiral lobe (10). The maximum gradient amplitude and slew rate used in this study were set to 12.8 mT/m and 127 mT/m/msec, respectively. Gradient delays between the apparent diffusion coefficient and the x and y gradients were 8 μsec and were corrected for in the reconstruction. Imaging along the third z spatial dimension was obtained with a phase-encoding gradient that was superimposed over the last z spoiler gradient of the LASER sequence, resulting in cylindrical 3D coverage of the k-space with a stack of spirals. Weighted phase encoding along k_z can be used for 3D k-space coverage with a stack of spirals to reduce baseline ringing of the point spread function along z. Details of the pulse sequence diagram are shown in Figure 1, *A*.

Data Processing

The spiral samples from each receive coil were two-dimensionally gridded with the Kaiser-Bessel kernel (18), and Cartesian data from all 32 coil elements were combined by using complex weights obtained with a short calibration pass performed during standard adjustments. No window settings were applied on the k-space or in the time domain. The entire reconstruction was implemented online by a graduate student in electrical engineering (B.A.G.) with 5 years of MR imaging experience using the Image Calculation Environment (ICE; Siemens). The reconstruction took less than 10 seconds for all spiral protocols performed with the 32-channel coil. The reconstructed spectra were subsequently available for inspection on the imager console.

Spectral fitting and metabolite quantification were performed (O.C.A.) with LCModel software *(http://s-provencher.com/)* (19) by using a custom-made basis set for the GOIA-W(16,4)-based LASER sequence (9) at an echo time of 45 msec and 3 T. Signal-to-noise ratio was estimated for several metabolites from the phase- and baseline-corrected spectra without any apodization. Maximum signal intensity was extracted for NAA, choline, creatine, glutamate and glutamine, and *myo*-inositol peaks, while noise was calculated as standard deviation of the baseline in a spectral region (0–0.5 ppm) free of signal with Matlab software (Mathworks, Natick, Mass). This SNR estimation (20) was preferred over that of the LCModel, which results in overestimation of noise and underestimation of SNR, since the standard deviation of the residual signal over the entire spectral region of interest (0.5–4.2 ppm) may contain real signal that was not properly fitted, thereby resulting in a higher apparent noise.

Statistical Analysis

Agreement between spiral- and phase-encoding protocols was analyzed (O.C.A.) by using the Bland-Altman method (20) to plot the difference between two types of measurements against their mean. Since involuntary head motion may influence the true limits of agreement (21), Bland-Altman analysis was performed for only phantom data. Metabolites from all voxels (n = 100) that had goodness of fit by

Figure 1

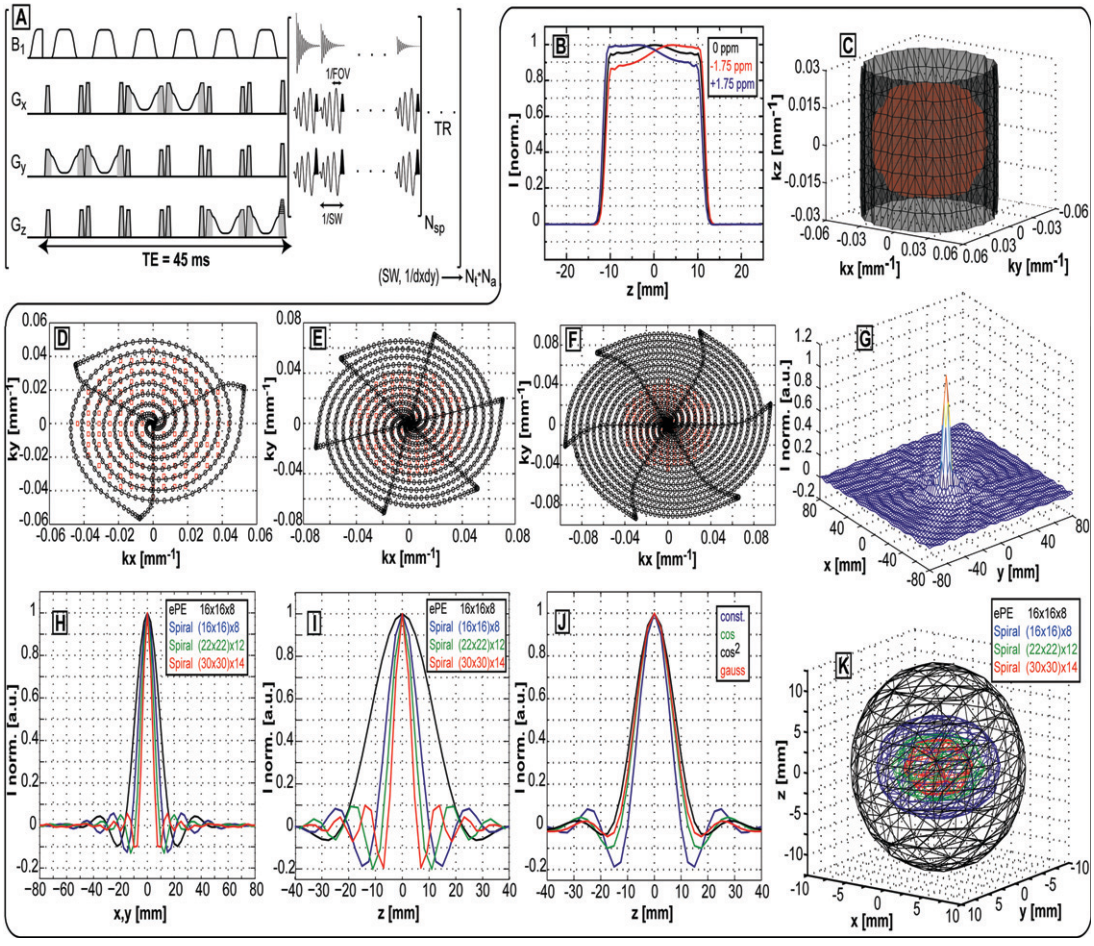

Figure 1: *A*, Adiabatic spiral 3D MR spectroscopic imaging sequence. LASER based on GOIA-W(16,4) pulses is used to select the VOI and spiral waveforms on x and y gradients to simultaneously acquire two spatial dimensions and one frequency dimension. Phase-encoding gradients superimposed on the last LASER spoiler encode the z dimension. *B*, Section profiles of GOIA-W(16,4) pulses for on-resonance (0 ppm) and off-resonance (+1.75 ppm, −1.75 ppm) spins. *C*, K-space volume sampled with stack-of-spirals (black) and elliptical phase-encoding (red) protocols for 16 × 16 × 8 matrix. *D–F*, Spiral trajectories for, *D*, 16 × 16; *E*, 22 × 22; and, *F*, 30 × 30 matrixes; red dots are elliptical phase-encoding points. *G*, Spiral point spread function (PSF) corresponding to 30 × 30 matrix. *H–I*, Projections of 3D PSF along x, y *(H)*, and z *(I)* directions for elliptical phase-encoding *(ePE)* and stack-of-spirals (spiral-acquired dimensions are specified inside brackets) protocols. *J*, PSF for weighted acquisition along z, using cos, $\cos^2$ and Gauss weighting. *K*, Isosurfaces obtained with 3D PSF at full-width half-maximum. In all simulations, the FOV of 160 × 160 × 80 mm and spectral window of 1.2 kHz at 3 T were assumed.

Cramer-Rao lower bounds smaller than 20% were used in the analysis. Spectra were normalized to account for the entire metabolic profile by calculating the parametric index of NAA over the sum of all metabolites (NAA/Sum), which was further used in the Bland-Altman plots to compare spiral- and phase-encoding measurements. In consideration of the regional variability of metabolite levels in humans, mean NAA/Sum and choline-to-creatine ratios were calculated over similar regions of interest in occipital white matter (healthy volunteers) and tumors (patients). Typically, metabolites from 10 voxels with acceptable goodness of fit (Cramer-Rao lower bounds <20%) were averaged to obtain the mean ratios. Because of the small number of subjects in each group, statistical comparison of healthy and tumor spectra was not attempted.

Results

Localization and PSF

Performance of LASER section selection and spiral encoding are shown (Fig 1, *B*–1, *K*). In Figure 1, *B*, measured section profiles of LASER localization are shown for on-resonance (0 ppm) and off-resonance (+1.75 ppm, −1.75 ppm) spins. Negligible (2.1%) chemical-shift

displacement error is obtained over a 3.5-ppm ^{1}H chemical-shift range of interest (0.7–4.2 ppm) at 3 T. Minimal section smearing due to gradient modulation is observed. Figure 1, *C*, shows the volume of k-space covered by the cylindrical stack of spirals and elliptical phase encoding for the 16 × 16 × 8 matrix. Angular spiral interleaves are shown for all in-plane matrixes (16 × 16 [Fig 1, *D*], 22 × 22 [Fig 1, *E*], and 30 × 30 [Fig 1, *F*]), and the red points on these images correspond to the elliptical phase-encoded 16 × 16 matrix. Figure 1, *G*, shows the PSF simulated for spiral trajectories from Figure 1, *F*. Projections of the 3D PSF along the x and y directions are shown in Figure 1, *H*, for the elliptical phase-encoding protocol and the spiral protocols. The elliptical phase-encoding protocol has a wider PSF than does any spiral protocol, even for the same matrix (16 × 16 × 8), as indicated by full-width half-maximum along the x and y directions. Full-width half-maximum was 16.1 mm for the elliptical phase-encoding protocol and 10.5 mm, 7.8 mm, and 6.2 mm for the 16 × 16 × 8, 22 × 22 × 12, and 30 × 30 × 14 spiral protocols, respectively. 3D PSF projections along the z direction are shown in Figure 1, *I*, for all protocols. The full-width half-maximum along the z direction is considerably wider for the elliptical phase-encoding protocol (25.4 mm) than for spiral protocols that use full phase encoding along the z direction (12.1 mm, 9.1 mm, and 7.6 mm for the 16 × 16 × 8, 22 × 22 × 12, and 30 × 30 × 14 spiral protocols, respectively). Because of less sampling of the k space for k_z, ringing of the PSF along the z direction is more obvious. Weighted phase encoding along z with cosine, cosine squared, and Gauss functions are compared in Figure 1, *J*, for the 16 × 16 × 8 spiral protocol. Reduced ringing is obtained naturally at the cost of a slightly wider central lobe, although this lobe is much narrower than that of elliptical phase encoding. The first positive side lobe amplitude is reduced by 50%, 55%, and 56%, while the full-width half-maximum of the main lobe is 14.2 mm, 14.6 mm, and 15.5 mm for cosine, Gauss, and cosine squared weighting, respectively. Sampling density-weighted acquisition is not feasible with full or elliptical phase-encoding protocols (Table 1) since taking more than one average results in impracticable long acquisition times for clinical imaging. In Figure 1, *K*, isosurfaces taken through 3D PSF at full-width half-maximum are shown for all protocols. The real voxel size of the elliptical phase-encoding protocol is larger than that of the spiral protocol, even for the same reconstructed 16 × 16 × 8 matrix. This effect of increased voxel size is a direct consequence of the more limited extent of k-space sampling with the elliptical phase-encoding scheme than that achieved with spiral acquisition. The real voxel volumes estimated from the integral of PSF for all in vivo protocols are given in Table 2. The real voxel volumes roughly correspond to cubes of 15.8-mm (elliptical phase-encoded protocol, 16 × 16 × 8 matrix), 10.5-mm (spiral-encoded protocol, 16 × 16 × 8 matrix), and 8.5-mm (spiral-encoded protocol, 22 × 22 × 14 matrix) isotropic dimensions, if we would like to think of it in terms of an image-based (nominal) voxel size.

Phantom Data

In Figure 2, the results obtained in both phantoms are presented. The leftmost column shows the double-layer phantom with a VOI (60 × 60 × 40 mm, AP-RL-HF direction) that was positioned inside the inner core and extended up to the oil-metabolite boundary. The elliptical phase-encoding protocol and five spiral phantom protocols (SP1–SP5) were all compared for accuracy of signal localization and signs of lipid contamination. The GOIA-W(16,4)-based LASER technique without outer-volume suppression bands was used to select VOIs with sharp margins that were maintained in all imaging protocols. Spectra for the entire FOV are shown, and no signs of lipid contamination or excitation are noticed in- or outside the VOI for any protocol.

A larger VOI (100 × 100 × 40 mm, AP-RL-HF direction) was selected in the uniform phantom. Spectral grids within the VOI and examples of spectra from the central voxels are shown in the three remaining columns of Figure 2. Data obtained with SP1–SP4 had sufficient SNR (>5) to enable us to clearly distinguish all metabolites observed in the phase-encoding data, including multiplets of coupled spins from less-concentrated metabolites, such as lactate and glutamate. The protocol with the highest spatial resolution (SP5) enabled us to identify the main metabolites (NAA, choline, creatine, *myo*-inositol), while the signals of glutamate and lactate were not clearly visible from the noise. NAA maps obtained for each protocol demonstrate the uniformity of excitation (standard deviations of 4%–5% for the 16 × 16 × 8 matrix, 7%–8% for the 22 × 22 × 12 matrix, and 10% for the 30 × 30 × 14 matrix). The apparent increase in nonuniformity at higher spatial resolution is due to higher noise contribution. The SP2–SP5 data have a lower SNR than phase-encoded data. This finding is consistent with the reduction in acquisition time and voxel size.

The results obtained with SP3 and SP4 suggest that these parameter settings might represent appropriate choices for in vivo 3D MR spectroscopic imaging for either very fast acquisition (1-cm^3 image voxel and four times faster) or higher spatial resolution and moderately fast acquisition (0.4-cm^3 image voxel and two times faster), respectively, when compared with the elliptical phase-encoded protocol (1-cm^3 image voxel).

MR Spectroscopic Imaging of Human Subjects

Figure 3 shows 3D MR spectroscopic images of the brain in a volunteer. A large VOI (100 × 80 × 40 mm, AP-RL-HF direction) was positioned centrally in the brain and was parallel to the anterior-posterior commissure line in the multiecho magnetization-prepared rapid acquisition gradient-echo anatomic image.

Spectral grids are shown for two sections within the VOI imaged with the elliptical phase-encoded protocol and SP2, SP3, and SP6. Examples of spectra from a central voxel are indicative of data quality. Spiral protocols revealed

Figure 2

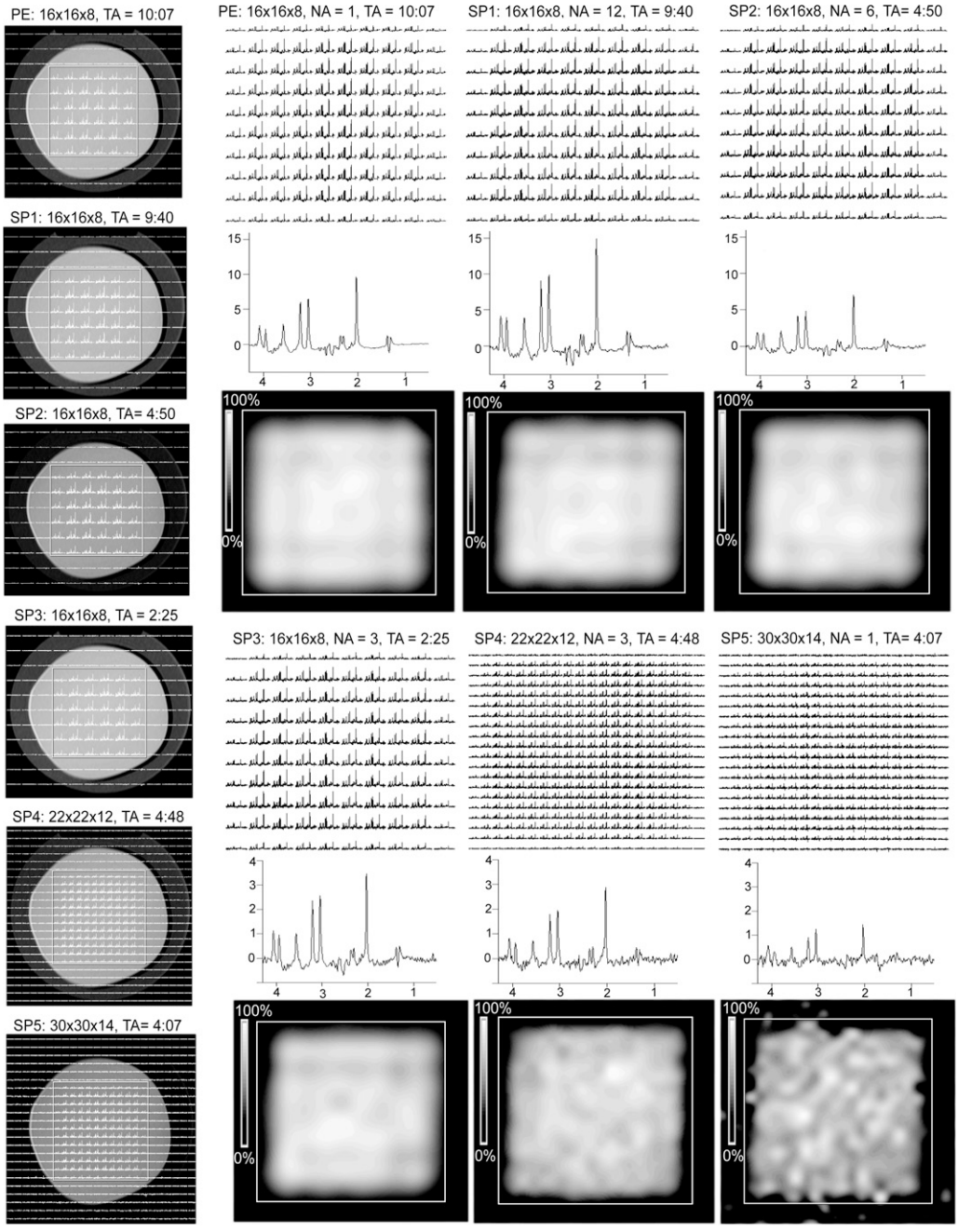

Figure 2: Elliptical phase-encoded and spiral (SP1-SP5) 3D MR spectroscopic imaging protocols in the double-layer and homogeneous brain phantoms. Left column: data from double-layer phantom show no signs of lipid contamination. Data from the homogeneous brain phantom are shown in the remaining columns. Entire spectral grids within the VOI (white rectangle), spectra from central voxels, and NAA maps are shown. *NA* = number of signals acquired, *TA* = acquisition time (specified in minutes, as obtained with a repetition time of 1000 msec).

spectra similar to those detected with the elliptical phase-encoding protocol. Multiplets of spin-coupled systems (*myo*-inositol and glutamate) are visible in all spectra. No signs of subcutaneous fat contamination are observed in any protocol. Sufficient SNR (>5) is obtained with spiral protocols of shorter acquisition times and higher spatial

Figure 3

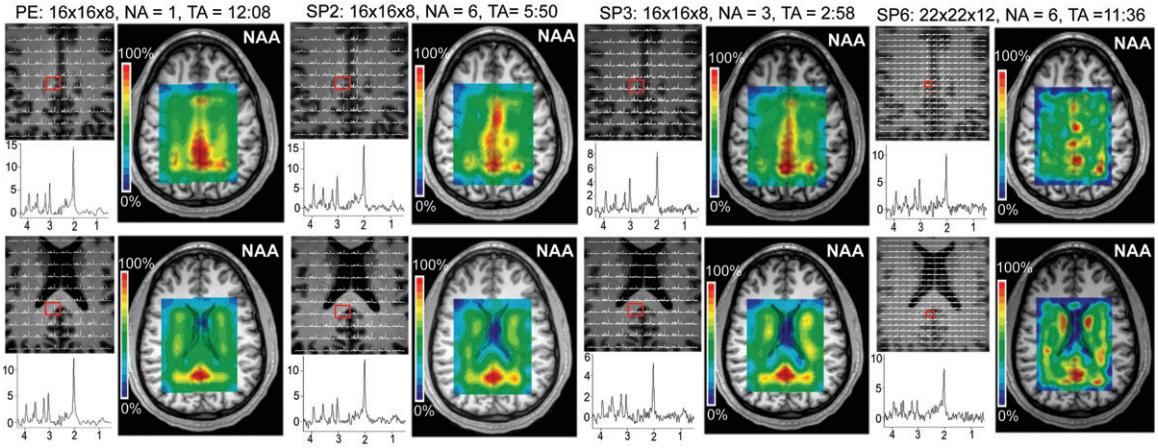

Figure 3: These 3D MR spectroscopic images of the brain were obtained in a volunteer with the elliptical phase-encoding protocol *(PE)* and SP2, SP3, and SP6. VOI spectral grids and examples of spectra from central voxels (red boxes) from two sections are shown. Sufficient SNR (>5) is obtained with spiral protocols at shorter acquisition times and higher spatial resolution. Spiral NAA maps show less partial volume effect by better delineation of ventricles. Acquisition time *(TA)* is specified in minutes (repetition time, 1200 msec).

Figure 4

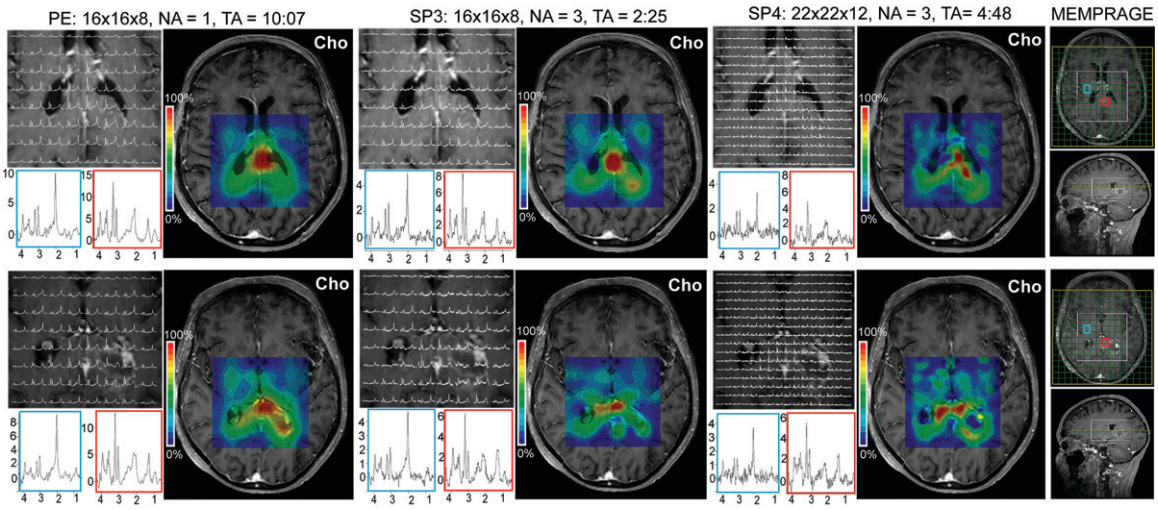

Figure 4: These 3D MR spectroscopic images were obtained in a patient with a brain tumor (glioblastoma) with the elliptical phase-encoding protocol *(PE)* and SP3 and SP4. Spectral grids and examples of spectra from voxels located in the healthy brain (blue boxes) and in the tumor (red boxes) are shown for two sections. Clinically adequate SNR (>5) is obtained with faster-acquisition and higher-spatial-resolution spiral protocols. Choline maps indicate that the active tumor and tumor necrosis are better delineated with high-spatial-resolution spiral protocols. Positions of FOV (yellow rectangle, green grid) and VOI (white rectangle) for each section are shown on axial and sagittal multiecho magnetization-prepared rapid acquisition gradient-echo cross sections. Acquisition time (TA) is specified in minutes (repetition time, 1000 msec).

resolution. NAA maps obtained with spiral and elliptical phase-encoding protocols show similar patterns; however, less partial volume effect is evident at higher spatial resolution (SP6) with better delineation of the ventricles.

Figure 4 presents the results obtained in a patient with a brain tumor (glioblastoma) with the elliptical phase-encoded protocol and SP3 and SP4. The VOI (80 × 80 × 40 mm, AP-RL-HF direction) was positioned on the contrast-enhanced T1-weighted multiecho magnetization-prepared rapid acquisition gradient-echo image to include the tumor and symmetric contralateral brain.

Spectra are shown for two sections corresponding to the middle of the enhancing tumor and the area above the enhancing tumor margin, respectively. The positions of the FOV and VOI for each section are shown on axial and sagittal multiecho magnetization-prepared rapid acquisition gradient-echo cross

Figure 5

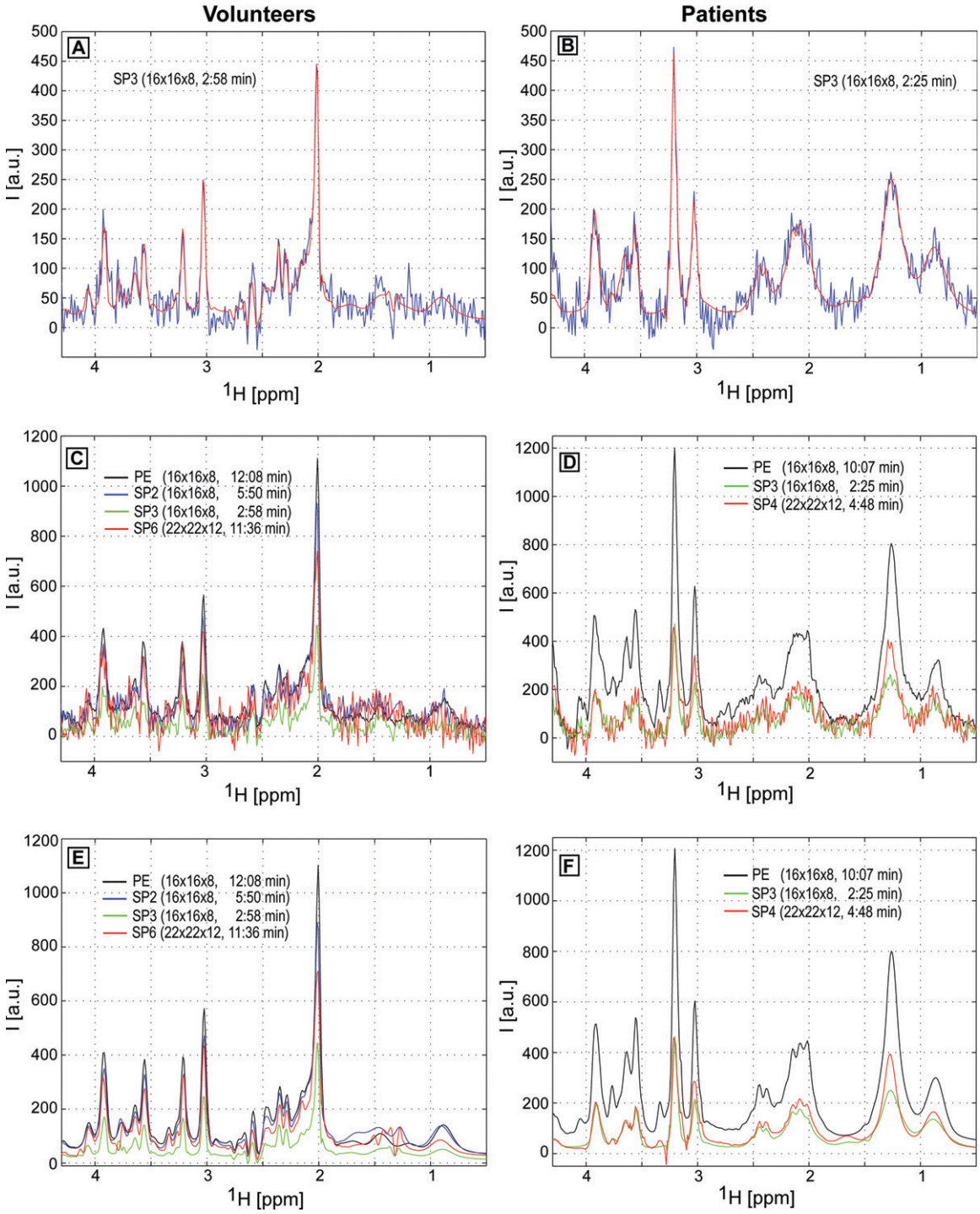

Figure 5: Overlays of spectra and LCModel fits for volunteers and patients with tumors. *A*, Measured spectra (blue) and LCModel fit (red) in a healthy volunteer obtained with a 16 × 16 × 8 matrix and 2-minute 58-second (repetition time, 1200 msec) spiral protocol. *B*, Measured spectrum (blue) and LCModel fit (red) in a patient with a brain tumor obtained with a 16 × 16 × 8 matrix and 2-minute 25-second (repetition time, 1000 msec) spiral protocol. *C*, *D*, Overlay of measured spectra recorded with all protocols in, *C*, a healthy volunteer and, *D*, a patient with a brain tumor. *E*, Overlay of LCModel fits for spectra from *C*. *F*, Overlay of LCModel fits for spectra from *D*. Similar voxel positions were chosen in all cases. *PE* = elliptical phase-encoding sequence.

Figure 6

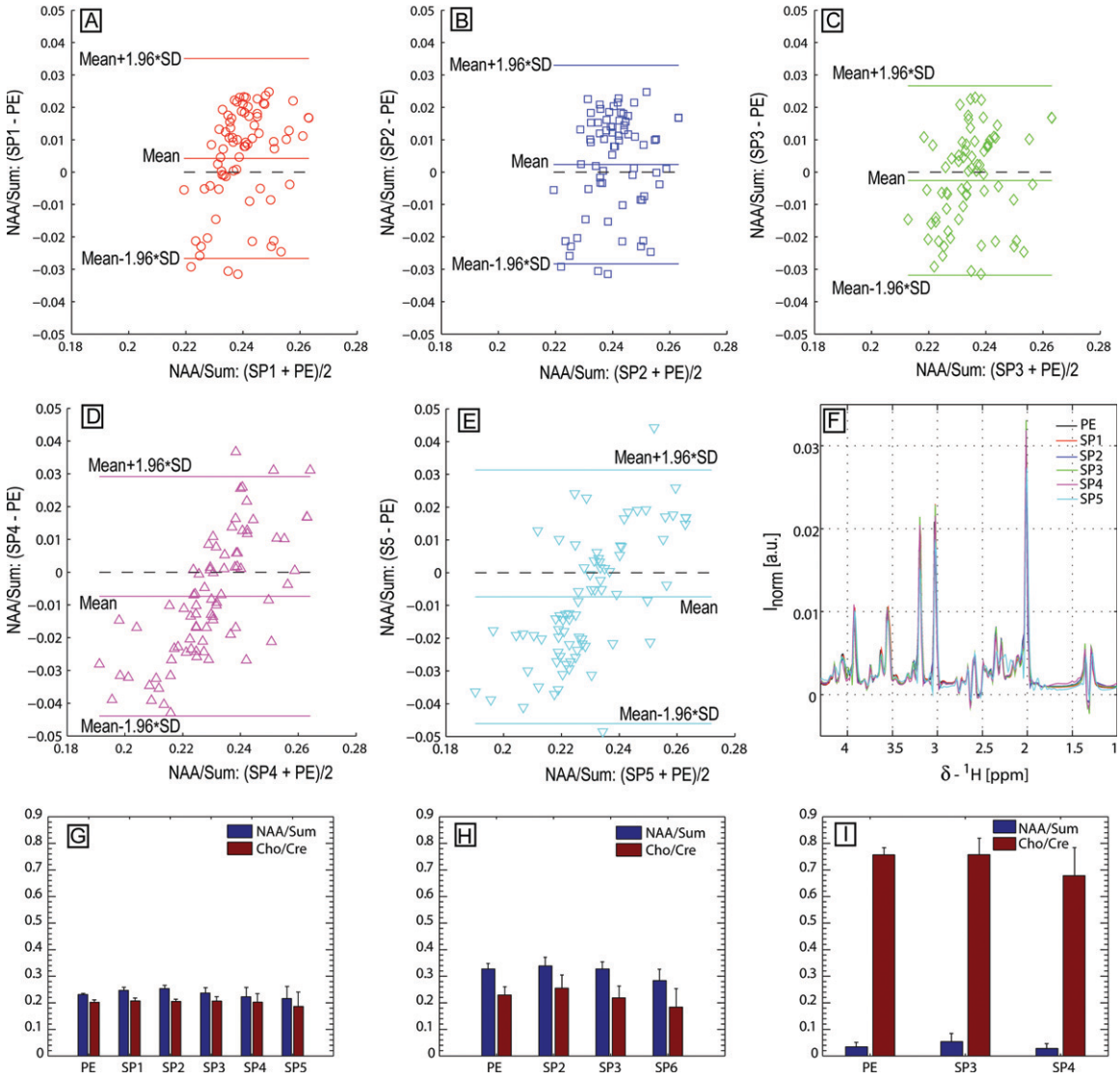

Figure 6: *A–E*, Bland-Altman plots indicate the limits of agreement between SP1–SP5 and elliptical phase-encoding *(PE)* measurements of NAA/Sum. *F*, Example of spectra normalized to area under spectral envelope (NAA/Sum). *G–I*, Mean values of NAA/Sum and choline-to-creatine *(Cho/Cre)* ratios are shown in, *G*, phantoms, *H*, volunteers, and, *I*, patients with tumors. Error bars = standard deviations.

sections. Examples of spectra from voxels in the healthy brain and tumor indicate that similar spectral profiles are detected with spiral and elliptical phase-encoding protocols. Metabolites detected with the elliptical phase-encoding protocol are preserved in spiral protocols, including spin-coupled metabolites (lactate and *myo*-inositol). Clinically adequate SNR (>5) is obtained with faster-acquisition and higher-spatial-resolution spiral protocols. The lower SNR of the spiral protocols compared with that of the elliptical phase-encoded protocol is consistent with the trade-off between SNR, imaging time, and spatial resolution. Choline maps are shown for both section positions. The overall choline distribution is similar in all protocols; however, the high-spatial-resolution spiral data (obtained with SP4) enable better separation of the areas of high choline tumor metabolism from ventricles or areas of necrosis. It is important to note that the choline maps show active tumor beyond the margins of the contrast-enhancing region.

Quality of in vivo measured spectra, spectral fitting, and statistical analysis are further presented in Figures 5 and 6. In Figure 5, examples of measured spectra and LCModel fits are shown for volunteers and patients. The upper row shows overlays of measured spectra and LCModel fits for SP3 ($16 \times 16 \times 8$; acquisition time, 2 minutes 25 seconds)

that were obtained in a volunteer (Fig 5, *A*) and a patient (Fig 5, *B*). The middle row shows overlaid spectra measured with all protocols in the same volunteer (Fig 5, *C*) and patient (Fig 5, *D*). The bottom row (Fig 5, *E*; 5, *F*) shows overlays of LCModel spectral fits corresponding to measured spectra of Figure 5, *C* and 5, *D*. All spectral features are preserved, and good LCModel fits (Cramer-Rao lower bounds of less than 20%) are obtained for all protocols.

SNR corresponding to main metabolites, such as NAA, choline, creatine, glutamate and glutamine, and *myo*-inositol, is given in Table 2. Adequate SNR was obtained for all protocols, with a minimum SNR of 5 considered adequate to reliably distinguish metabolite peaks from noise (Rose criterion [20]). SNR seems to decrease in a less-than-linear fashion as spatial resolution improves. When accounting for the scaling factor due to reduced voxel sizes, higher SNR is obtained per square root of time with spiral protocols than with the elliptical phase-encoding protocol. This effect is explained by a combination of two factors: *(a)* less T2* signal decay for smaller voxels because of less B_0 inhomogeneity, as shown by improvement in line width from 4.8 Hz to 3.5 Hz, and *(b)* partial volume effects leading to more contamination for bigger voxels with cerebrospinal fluid signal that does not contain metabolites. Similar observations about SNR change with decreasing voxel size have been documented for in vivo spectroscopy (22).

Figure 6, *A*–6, *E* shows Bland-Altman plots of phantom data acquired with SP1, SP2, SP3, SP4, and SP5 as compared with phantom data acquired with the elliptical phase-encoding protocol. The mean difference of the NAA/Sum index has small positive biases for SP1 (0.004) and SP2 (0.002) and negative biases for SP3 (−0.002), SP4 (−0.007), and SP5 (−0.007). The confidence intervals for the limits of agreement are narrower (12%–13% of the mean 0.242) for SP1, SP2, and SP3 and slightly wider for SP4 (16% of the mean 0.231) and SP5 (18% of the mean 0.231). Because of their different PSFs, elliptical phase-encoding and spiral protocols are expected to yield slightly different estimations of metabolite levels, with a smaller difference for the same matrix size (SP1, SP2, and SP3 with a 16 × 16 × 8 matrix) and larger difference for higher-spatial-resolution matrixes (SP4, 22 × 22 × 12 matrix; SP5, 30 × 30 × 14 matrix). Figure 6, *F*, shows an example of spectra normalized to total area under the spectral envelope within the range of 4.2–1.0 ppm. Figure 6, *G*–6, *I*, shows plots for the mean values of NAA/Sum and choline-to-creatine ratios in phantoms (Fig 6, *G*), volunteers (Fig 6, *H*), and patients with a tumor (Fig 6, *I*). Although a large difference can be noticed between metabolite levels in healthy subjects (NAA/Sum, 0.28–0.34; choline-to-creatine ratio, 0.19–0.24) and those in patients with a tumor (NAA/Sum, 0.03–0.06; choline-to-creatine ratio, 0.69–0.76), the significance needs to be considered in light of the small sample size in each group.

Discussion

In this work, we have shown that the added value of fully adiabatic localization and spiral encoding can considerably improve the quality of 3D MR spectroscopic imaging in a standard clinical MR set-up. Protocols that perform robustly in clinical practice can be designed, and high-spatial-resolution 3D MR spectroscopic imaging data can be obtained reliably within a feasible imaging time.

The fully adiabatic LASER excitation selects all three dimensions by using adiabatic pulses that have a much wider bandwidth and a lower SAR than those used previously (23). Adiabatic radiofrequency pulses have been shown (8,9,24,25) by many investigators to reduce chemical-shift displacement error and provide sharp and uniform excitation, even in the presence of an inhomogeneous B_1 field. However, the power deposition associated with typical adiabatic pulses is higher than that for conventional pulses. The SAR and maximum B_1 field of adiabatic pulses can be lowered considerably by using gradient modulation (9,24–27). Gradient-offset independent adiabaticity pulses (24) have a constant adiabatic factor over very large inversion bandwidths. Wideband uniform rate and smooth truncation (15) modulation of the gradient-offset independent adiabaticity pulses, known as GOIA-W(16,4), (9) were shown to have improved performance of clinical 3-T imagers, with fewer eddy current artifacts. In terms of maximum B_1, GOIA-W(16,4) pulses compare well with nonadiabatic pulses, such as Mao pulses (28) used in point-resolved spatially localized spectroscopy, which need higher B_1 (1 kHz) for a much smaller bandwidth (1.2 kHz, equivalent to 38% chemical-shift displacement error) and longer duration (5.2 msec).

Higher-spatial-resolution data obtained with spiral acquisition have less partial volume effect and can be used to better delineate underlying disease, such as brain tumors. Fast spectroscopic imaging that simultaneously acquires frequency and spatial dimensions was proposed by Mansfield (29) and was soon followed by in vivo applications of time-variable gradients for spectroscopic imaging (30). To date, two of the most used acquisition methods are based on echo planar (proton echo-planar spectroscopic imaging [31–34] and echo-planar spectroscopic imaging [35–37]) and spiral (10,38–40) spectroscopic imaging trajectories. Rosette (41), radial (42), or more complicated (30) trajectories have been described but have been used less frequently. Spiral gradient waveforms vary smoothly compared with the proton echo-planar spectroscopic imaging or echo-planar spectroscopic imaging protocols and efficiently use the gradient hardware in terms of rise time, maximum amplitude, and slew rate. Importantly, spiral trajectories accelerate acquisition in two spatial dimensions by simultaneously encoding the k_x, k_y, and k_f space, while the proton echo-planar spectroscopic imaging and echo-planar spectroscopic imaging approaches accelerate the acquisition only along one spatial dimension by simultaneously encoding the k_x and k_f space. Hence, spiral acquisition can be twice as fast compared with proton echo-planar spectroscopic imaging

and echo-planar spectroscopic imaging. Historically, spiral acquisitions imply several challenges: They require the design of a suitable trajectory that fulfills all the constraints and the choice of two-dimensional gridding algorithm. They may have more pronounced artifacts (43) caused by experimental imperfections, such as gradient deviations, resonance offset contributions, and concomitant field effects than usually obtained for echo-planar–based methods. However, when chemical shift is resolved, as in MR spectroscopic imaging, the resonance offset contribution can be separated. With the latest developments in gradient hardware and efficient online reconstruction algorithms, these challenges play a lesser role. All the spectral information present in phase-encoded data is retained in spiral protocols. SNR loss at high spatial resolution is less than linear with decreasing voxel sizes due to longer local T2* times for smaller voxels and less contamination with cerebrospinal fluid signal.

While fast 3D MR spectroscopic imaging has been performed with conventional excitation schemes (stimulated-echo acquisition mode, point-resolved spatially localized spectroscopy, or spin-echo imaging) (10,31,39), its combination with adiabatic excitation has been less investigated (11,12). Semiadiabatic excitation has been used in proton echo-planar spectroscopic imaging (11) and spiral (12) MR spectroscopic imaging. Although the semi-LASER excitation based on conventional adiabatic pulses that was used in previous studies (11,12) improves the situation in the x and y planes, it is certainly not optimal for use in the z direction, which is selected with a conventional pulse.

Selection of the volume of interest with LASER based on GOIA-W(16,4) pulses provides uniform excitation with sharp edges and virtually no chemical-shift displacement error because of much larger bandwidth compared to bandwidth with semi-LASER, PRESS, and STEAM excitations. Use of outer volume suppression for LASER excitation is not necessary to reduce lipid contamination from subcutaneous fat. This helps the operator in setting up protocols faster and enables the VOI to be positioned closer to the skull, as is required in many cases because of the location of the lesion. Compared with point-resolved spatially localized spectroscopy or stimulated-echo acquisition mode imaging, LASER refocuses better J evolution for spin-coupled metabolites, such as glutamate, *myo*-inositol, and lactate, resulting in better SNR and less line shape modulation. The SAR associated with the use of GOIA-W(16,4)–based LASER is lower than SAR of semi-LASER using conventional adiabatic pulses, and enables short repetition times (1000–1200 msec) at 3 T, which keep the total imaging time within feasible limits.

Several limitations and further improvement of the current work are worth mentioning. Conventional phase encoding of the k-space can be accelerated by using parallel imaging (44–46) and compressed sensing (47) methods. Typical acceleration factors in parallel imaging and compressed sensing enable imaging times that are four to 20 times faster and that are comparable to or slower than those that can be achieved with spiral encoding. On the other hand, parallel imaging with high acceleration factors relies on phased arrays with a large number of receive coils; however, spiral imaging does not depend on this. Iterative reconstruction of compressed sensing data are typically performed off-line and need powerful computational resources for short reconstruction times (48,49). These extra hardware requirements are not yet commonly available for most clinical sites. However, spiral MR spectroscopic imaging or proton echo-planar spectroscopic imaging can be further accelerated, if necessary, by using parallel imaging (45,50,51) or compressed sensing (52–55) methods. Furthermore, variable density spirals with matching apodization have been used to reduce ringing and side lobes of PSF (56) with minimal SNR tradeoffs, k-space coverage with spherical stacks of spirals can be used to reduce imaging time even further (10), and self-rewinding out-and-in spiral trajectories could eliminate the need for rewinder gradients (57), although they would reduce the spectral window in half. Real-time motion correction and shim update (21) can be realized for MR spectroscopic imaging to improve robustness of clinical examinations.

A potential limitation in our approach results from the use of a rectangular VOI which excludes regions of cortical gray matter when compared with slice selection with full coverage (58). LASER can be easily modified into a slab-selecting sequence by using only a pair of adiabatic pulses while maintaining the advantages of adiabatic excitation. Although this approach would decrease SAR and echo times, it would require improved saturation bands (59) and automatic placement of the outer volume suppression (60) or optimized inversion recovery (61,62) for efficient lipid suppression, with the associated decrease of SNR in the last case. On the other hand, the quality of spectra obtained with LASER localization can be attractive, especially when disease (brain tumors, multiple sclerosis) is located in white matter or in subcortical gray matter and the limbic system (neuropsychiatric and neurodegenerative disorders).

In conclusion, we designed an adiabatic-excited and spiral-encoded 3D MR spectroscopic imaging sequence that performs robustly on clinical imagers equipped with standard hardware and yields precise excitation, shorter acquisition times (four times shorter), and/or higher spatial resolution (85% smaller voxels) for patient examination. These advancements may enable 3D MR spectroscopic imaging to be performed more routinely in a wide variety of clinical sites and to obtain reliable metabolic information that could improve the diagnosis of disease and care of patients.

Acknowledgments: We gratefully acknowledge Elfar Adalsteinsson, PhD, Department of Electrical Engineering and Computer Science, Massachusetts Institute of Technology, for extremely valuable support regarding spiral design and useful comments on results; Marjanska Malgorzata, PhD, Center for Magnetic Resonance Research, University of Minnesota, for help with building the LCModel basis set for LASER excitation;

and Kim Mouridsen, PhD, Center for Functionally Integrative Neuroscience, University of Aarhus, for advice regarding statistical analysis. We also thank Elizabeth Gerstner, MD and Tracy Batchelor, MD, Pappas Center for Neuro-Oncology, Department of Neurology, Massachusetts General Hospital, for access to patients with glioblastoma. Discussions with Nouha Salibi, PhD, Thomas Benner, PhD, and Michael Hamm, Dipl Eng, Siemens Medical Solutions, are also gratefully acknowledged.

Disclosures of Potential Conflicts of Interest: O.C.A. No potential conflicts of interest to disclose. **B.A.G.** No potential conflicts of interest to disclose. **A.G.S.** Financial activities related to the present article: none to disclose. Financial activities not related to the present article: is a consultant to Siemens. Other relationships: none to disclose.

References

1. Gillard J, Waldman A, Barker P, eds. Clinical MR neuroimaging: diffusion, perfusion, spectroscopy. Cambridge, England: Cambridge University Press, 2005.
2. Nelson SJ. Multivoxel magnetic resonance spectroscopy of brain tumors. Mol Cancer Ther 2003;2(5):497–507.
3. Mountford CE, Stanwell P, Lin A, Ramadan S, Ross B. Neurospectroscopy: the past, present and future. Chem Rev 2010;110(5):3060–3086.
4. Barker PB, Bizzi A, De Stefano N, Gullapalli RP, Lin DDM. Clinical MR spectroscopy: techniques and applications. Cambridge, England: Cambridge University Press, 2010.
5. Mettler FA Jr, Guiberteau MJ. Essentials of nuclear medicine imaging. Philadelphia, Pa: Saunders Elsevier, 2006.
6. Bottomley PA. Spatial localization in NMR spectroscopy in vivo. Ann N Y Acad Sci 1987;508:333–348.
7. Brown TR, Kincaid BM, Ugurbil K. NMR chemical shift imaging in three dimensions. Proc Natl Acad Sci U S A 1982;79(1):3523–3526.
8. Garwood M, DelaBarre L. The return of the frequency sweep: designing adiabatic pulses for contemporary NMR. J Magn Reson 2001;153(2):155–177.
9. Andronesi OC, Ramadan S, Ratai EM, Jennings D, Mountford CE, Sorensen AG. Spectroscopic imaging with improved gradient modulated constant adiabaticity pulses on high-field clinical scanners. J Magn Reson 2010;203(2):283–293.
10. Adalsteinsson E, Irarrazabal P, Topp S, Meyer C, Macovski A, Spielman DM. Volumetric spectroscopic imaging with spiral-based k-space trajectories. Magn Reson Med 1998;39(6):889–898.
11. Scheenen TW, van der Moortele PF, Adriany G, van der Kouwe A, Otazo R, Posse S. High spatial resolution short TE proton-echo-planar-spectroscopic-imaging (PEPSI) in human brain at 7 Tesla using B1-compensation and adiabatic refocusing [abstr]. In: Proceedings of the Sixteenth Meeting of the International Society for Magnetic Resonance in Medicine. Berkeley, Calif: International Society for Magnetic Resonance in Medicine, 2008; 1593.
12. Tachrount M, Lamalle L, Warnking J, Segebarth C. Short TE volumetric spiral 1H MR spectroscopic imaging of the human brain at 3T using semi-LASER [abstr]. In: Proceedings of the Seventeenth Meeting of the International Society for Magnetic Resonance in Medicine. Berkeley, Calif: International Society for Magnetic Resonance in Medicine, 2009; 4312.
13. Maudsley AA, Matson GB, Hugg JW, Weiner MW. Reduced phase encoding in spectroscopic imaging. Magn Reson Med 1994;31(6):645–651.
14. van der Kouwe AJ, Benner T, Salat DH, Fischl B. Brain morphometry with multiecho MPRAGE. Neuroimage 2008;40(2):559–569.
15. Kupce E, Freeman R. Adiabatic pulses for wideband inversion and broadband decoupling. J Magn Reson A 1995;115(2):273–276.
16. Tannús A, Garwood M. Improved performance of frequency-swept pulses using offset-independent adiabaticity. J Magn Reson A 1996;120(1):133–137.
17. Ogg RJ, Kingsley PB, Taylor JS. WET, a T1- and B1-insensitive water-suppression method for in vivo localized 1H NMR spectroscopy. J Magn Reson B 1994;104(1):1–10.
18. Beatty PJ, Nishimura DG, Pauly JM. Rapid gridding reconstruction with a minimal oversampling ratio. IEEE Trans Med Imaging 2005;24(6):799–808.
19. Provencher SW. Estimation of metabolite concentrations from localized in vivo proton NMR spectra. Magn Reson Med 1993;30(6):672–679.
20. Bushberg JT, Seibert JA, Leidholdt EM Jr, Boone JM. The essential physics of medical imaging. Philadelphia, Pa: Lippincott Williams & Wilkins, 2006.
21. Hess AT, Andronesi OC, Dylan Tisdall M, Gregory Sorensen A, van der Kouwe AJ, Meintjes EM. Real-time motion and B(0) correction for localized adiabatic selective refocusing (LASER) MRSI using echo planar imaging volumetric navigators. NMR Biomed doi: 10.1002/nbm.1756. Published online July 28, 2011. Accessed July 28, 2011.
22. Gruber S, Mlynárik V, Moser E. High-resolution 3D proton spectroscopic imaging of the human brain at 3 T: SNR issues and application for anatomy-matched voxel sizes. Magn Reson Med 2003;49(2):299–306.
23. Scheenen TW, Klomp DW, Wijnen JP, Heerschap A. Short echo time 1H-MRSI of the human brain at 3T with minimal chemical shift displacement errors using adiabatic refocusing pulses. Magn Reson Med 2008;59(1):1–6.
24. Tannús A, Garwood M. Adiabatic pulses. NMR Biomed 1997;10(8):423–434.
25. Ordidge RJ, Wylezinska M, Hugg JW, Butterworth E, Franconi F. Frequency offset corrected inversion (FOCI) pulses for use in localized spectroscopy. Magn Reson Med 1996;36(4):562–566.
26. Conolly S, Nishimura D, Macovski A, Glover G. Variable-rate selective excitation. J Magn Reson 1988;78(3):440–458.
27. Kinchesh P, Ordidge RJ. Spin-echo MRS in humans at high field: LASER localisation using FOCI pulses. J Magn Reson 2005;175(1):30–43.
28. Mao JT, Mareci TH, Scott KN, Andrew ER. Selective inversion radiofrequency pulses by optimal-control. J Magn Reson 1986;70:310–318.
29. Mansfield P. Spatial mapping of the chemical shift in NMR. Magn Reson Med 1984;1(3):370–386.
30. Adalsteinsson E, Irarrazabal P, Spielman DM, Macovski A. Three-dimensional spectroscopic imaging with time-varying gradients. Magn Reson Med 1995;33(4):461–466.
31. Posse S, Tedeschi G, Risinger R, Ogg R, Le Bihan D. High speed 1H spectroscopic imaging in human brain by echo planar spatial-spectral encoding. Magn Reson Med 1995;33(1):34–40.
32. Bustillo JR, Rowland LM, Chen H, et al. Glutamatergic dysfunction in early schizophrenia: 4TESLA 1H-MRS single-voxel and proton-echo planar spectroscopic imaging (PEPSI) studies. Schizophr Bull 2007;33:392–393.
33. Heide AC, Kraft GH, Slimp JC, et al. Cerebral N-acetylaspartate is low in patients with multiple sclerosis and abnormal visual evoked potentials. AJNR Am J Neuroradiol 1998;19(6):1047–1054.
34. Chu A, Alger JR, Moore GJ, Posse S. Proton echo-planar spectroscopic imaging with highly effective outer volume suppression using combined presaturation and spatially

selective echo dephasing. Magn Reson Med 2003;49(5):817–821.

35. Ebel A, Maudsley AA. Improved spectral quality for 3D MR spectroscopic imaging using a high spatial resolution acquisition strategy. Magn Reson Imaging 2003;21(2):113–120.
36. Maudsley AA, Domenig C, Ramsay RE, Bowen BC. Application of volumetric MR spectroscopic imaging for localization of neocortical epilepsy. Epilepsy Res 2010;88(2-3):127–138.
37. Ebel A, Soher BJ, Maudsley AA. Assessment of 3D proton MR echo-planar spectroscopic imaging using automated spectral analysis. Magn Reson Med 2001;46(6):1072–1078.
38. Kim DH, Gu M, Cunningham C, et al. Fast 3D (1)H MRSI of the corticospinal tract in pediatric brain. J Magn Reson Imaging 2009;29(1):1–6.
39. Gu M, Kim DH, Mayer D, Sullivan EV, Pfefferbaum A, Spielman DM. Reproducibility study of whole-brain 1H spectroscopic imaging with automated quantification. Magn Reson Med 2008;60(3):542–547.
40. Adalsteinsson E, Langer-Gould A, Homer RJ, et al. Gray matter N-acetyl aspartate deficits in secondary progressive but not relapsing-remitting multiple sclerosis. AJNR Am J Neuroradiol 2003;24(10):1941–1945.
41. Schirda CV, Tanase C, Boada FE. Rosette spectroscopic imaging: optimal parameters for alias-free, high sensitivity spectroscopic imaging. J Magn Reson Imaging 2009;29(6):1375–1385.
42. Sarty GE. Single TrAjectory radial (STAR) imaging. Magn Reson Med 2004;51(3):445–451.
43. Block KT, Frahm J. Spiral imaging: a critical appraisal. J Magn Reson Imaging 2005;21(6):657–668.
44. Dydak U, Weiger M, Pruessmann KP, Meier D, Boesiger P. Sensitivity-encoded spectroscopic imaging. Magn Reson Med 2001;46(4):713–722.
45. Mayer D, Kim DH, Spielman DM, Bammer R. Fast parallel spiral chemical shift imaging at 3T using iterative SENSE reconstruction. Magn Reson Med 2008;59(4):891–897.
46. Bonekamp D, Smith MA, Zhu H, Barker PB. Quantitative SENSE-MRSI of the human brain. Magn Reson Imaging 2010;28(3):305–313.
47. Lustig M, Donoho DL, Santos JM, Pauly JM. Compressed sensing MRI. IEEE Signal Process Mag 2008;25(2):72–82.
48. Lai P, Lustig M, Brau AC, Vasanawala S, Beatty PJ, Alley M. Efficient L1SPIRiT reconstruction (ESPIRiT) for highly accelerated 3D volumetric MRI with parallel imaging and compressed sensing. In: Proceedings of the Joint Annual Meeting ISMRM-ESMRMB, Stockholm, Sweden, 2010; 345.
49. Murphy M, Keutzer K, Vasanawala S, Lustig M. Clinically feasible reconstruction time for L1-SPIRiT parallel imaging and compressed sensing MRI. In: Proceedings of the Joint Annual Meeting ISMRM-ESMRMB, Stockholm, Sweden, 2010; 4854.
50. Tsai SY, Otazo R, Posse S, et al. Accelerated proton echo planar spectroscopic imaging (PEPSI) using GRAPPA with a 32-channel phased-array coil. Magn Reson Med 2008;59(5):989–998.
51. Lin FH, Tsai SY, Otazo R, et al. Sensitivity-encoded (SENSE) proton echo-planar spectroscopic imaging (PEPSI) in the human brain. Magn Reson Med 2007;57(2):249–257.
52. Hu S, Lustig M, Balakrishnan A, et al. 3D compressed sensing for highly accelerated hyperpolarized (13)C MRSI with in vivo applications to transgenic mouse models of cancer. Magn Reson Med 2010;63(2):312–321.
53. Hu S, Lustig M, Chen AP, et al. Compressed sensing for resolution enhancement of hyperpolarized 13C flyback 3D-MRSI. J Magn Reson 2008;192(2):258–264.
54. Mayer D, Yen YF, Tropp J, Pfefferbaum A, Hurd RE, Spielman DM. Application of subsecond spiral chemical shift imaging to real-time multislice metabolic imaging of the rat in vivo after injection of hyperpolarized 13C1-pyruvate. Magn Reson Med 2009;62(3):557–564.
55. Mayer D, Yen YF, Levin YS, et al. In vivo application of sub-second spiral chemical shift imaging (CSI) to hyperpolarized 13C metabolic imaging: comparison with phase-encoded CSI. J Magn Reson 2010;204(2):340–345.
56. Adalsteinsson E, Star-Lack J, Meyer CH, Spielman DM. Reduced spatial side lobes in chemical-shift imaging. Magn Reson Med 1999;42(2):314–323.
57. Hiba B, Faure B, Lamalle L, Décorps M, Ziegler A. Out-and-in spiral spectroscopic imaging in rat brain at 7 T. Magn Reson Med 2003;50(6):1127–1133.
58. Barker PB, Gillard JH, van Zijl PC, et al. Acute stroke: evaluation with serial proton MR spectroscopic imaging. Radiology 1994;192(3):723–732.
59. Tran TK, Vigneron DB, Sailasuta N, et al. Very selective suppression pulses for clinical MRSI studies of brain and prostate cancer. Magn Reson Med 2000;43(1):23–33.
60. Martínez-Ramón M, Gallardo-Antolín A, Cid-Sueiro J, et al. Automatic placement of outer volume suppression slices in MR spectroscopic imaging of the human brain. Magn Reson Med 2010;63(3):592–600.
61. Ebel A, Govindaraju V, Maudsley AA. Comparison of inversion recovery preparation schemes for lipid suppression in 1H MRSI of human brain. Magn Reson Med 2003;49(5):903–908.
62. Balchandani P, Spielman D. Fat suppression for 1H MRSI at 7T using spectrally selective adiabatic inversion recovery. Magn Reson Med 2008;59(5):980–988.